



HAL
open science

Influence of Microstructure and Surface Roughness on Oxidation Kinetics at 500–600 °C of Ti–6Al–4V Alloy Fabricated by Additive Manufacturing

Antoine Casadebaigt, Jonathan Hugues, Daniel Monceau

► **To cite this version:**

Antoine Casadebaigt, Jonathan Hugues, Daniel Monceau. Influence of Microstructure and Surface Roughness on Oxidation Kinetics at 500–600 °C of Ti–6Al–4V Alloy Fabricated by Additive Manufacturing. *Oxidation of Metals*, 2018, 90 (5-6), pp.633-648. 10.1007/s11085-018-9859-0 . hal-01992320

HAL Id: hal-01992320

<https://hal.science/hal-01992320>

Submitted on 24 Jan 2019

HAL is a multi-disciplinary open access archive for the deposit and dissemination of scientific research documents, whether they are published or not. The documents may come from teaching and research institutions in France or abroad, or from public or private research centers.

L'archive ouverte pluridisciplinaire **HAL**, est destinée au dépôt et à la diffusion de documents scientifiques de niveau recherche, publiés ou non, émanant des établissements d'enseignement et de recherche français ou étrangers, des laboratoires publics ou privés.





Open Archive Toulouse Archive Ouverte (OATAO)

OATAO is an open access repository that collects the work of Toulouse researchers and makes it freely available over the web where possible

This is an author's version published in: <http://oatao.univ-toulouse.fr/21418>

Official URL: <https://doi.org/10.1007/s11085-018-9859-0>

To cite this version:

Casadebaigt, Antoine  and Hugues, Jonathan and Monceau, Daniel  *Influence of Microstructure and Surface Roughness on Oxidation Kinetics at 500–600 °C of Ti–6Al–4V Alloy Fabricated by Additive Manufacturing*. (2018) *Oxidation of Metals*, 90 (5-6). 633-648. ISSN 0030-770X

Any correspondence concerning this service should be sent to the repository administrator: tech-oatao@listes-diff.inp-toulouse.fr

Influence of Microstructure and Surface Roughness on Oxidation Kinetics at 500–600 °C of Ti–6Al–4V Alloy Fabricated by Additive Manufacturing

Antoine Casadebaigt^{1,2} · Jonathan Hugues¹ · Daniel Monceau²

Abstract

Ti–6Al–4V alloy (TA6V) is the most commonly used titanium-based alloy and is usually manufactured by casting, forging or rolling. Additive manufacturing is a new way of processing metal alloys; it is currently used for production purposes. This study focuses on the microstructure and oxidation kinetics of Ti–6Al–4V fabricated by laser beam melting. Some samples were HIP-treated (hot isostatic pressure). Ti–6Al–4V rolled and annealed was used as a reference material. Ti–6Al–4V fabricated by LBM exhibited prior β grains elongated in the building direction with fully acicular martensite, α' . Isothermal oxidations were performed at 500, 550 and 600 °C for durations of 100, 200 and 500 h. The oxidation kinetics followed a parabolic law. The weight gain of as-built LBM samples was twice as high as that of ground LBM samples of Ti–6Al–4V, although both sets had the same oxide layer thickness and depth of oxygen diffusion in the alloy. Ground LBM samples presented an oxidation rate close to that of conventional rolled and annealed Ti–6Al–4V alloys. It was shown the higher weight gain of LBM-produced Ti–6Al–4V samples was mainly due to their higher specific area and to the oxidation of partially melted powder on their surface.

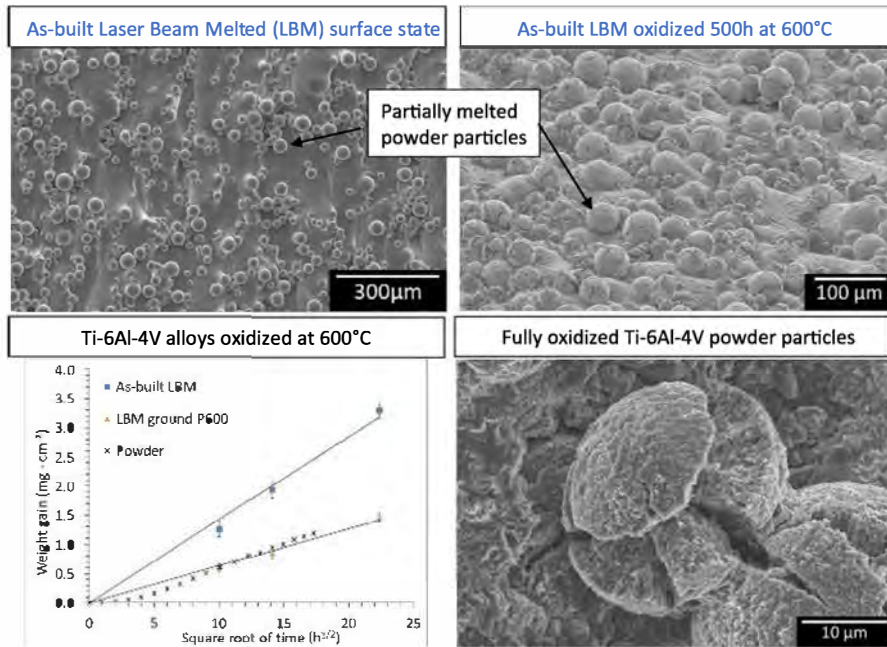
✉ Antoine Casadebaigt

antoine.casadebaigt@ensiacet.fr

¹ IRT Saint Exupéry, 3 rue Tarfaya, 31405 Toulouse Cedex 4, France

² CIRIMAT, CNRS, INPT, UPS, ENSIACET, Université de Toulouse, 4 allée Emile Monso, BP-44362, 31030 Toulouse Cedex 4, France

Graphical Abstract



Keywords SLM · TA6V · Oxidation · Titanium · High temperature · Additive manufacturing

Introduction

Titanium alloys are widely used in aeronautic applications due to their good density-specific mechanical properties and aqueous corrosion resistance. However, applications for titanium alloys are often limited to temperatures below 550 °C, e.g. 400 °C for Ti-6Al-4V (wt%) [1]. This is due to the relatively fast rate of external oxide layer (OL) growth at high temperature and more importantly to the very high oxygen solubility in the metal. This high oxygen solubility leads to an oxygen diffusion zone (ODZ) beneath the external oxide scale provoking a loss of ductility [2, 3]. Ti-6Al-4V represents nearly 60% of titanium alloys produced [1] and is frequently used in jet-engine components and aircraft structural components [4].

Laser beam melting (LBM) also named selective laser melting (SLM) is one of the additive manufacturing processes that emerged in the late 1980s and early 1990s [5]. The process has been widely described in the literature [6–8]. This technique enables the manufacturing of nearly dense metal parts with complex geometries and is currently under development for mass production [9–12]. The layer-by-layer process of the LBM allows the manufacturing of complex geometry parts, which are

impossible to build with more conventional manufacturing processes such as forging or casting [13]. Moreover, hot working and machining used in traditional processes result in a high buy-to-fly ratio—defined as the mass of raw material purchased to manufacture a part compared to the final part’s mass in flight—e.g. the mid-fuselage bulkhead of the USF-22 [14]. LBM process reduces the amount of wasted matter compared to machining processes.

Most reports involving titanium alloys fabricated by LBM concentrate on microstructure and mechanical properties [9, 11, 12, 15–18]. Up to now, no study has focused on high-temperature oxidation behaviour of LBM-produced Ti–6Al–4V alloy. A single study discussing the high-temperature oxidation behaviour of a titanium alloy (Ti–5.5Al–3.4Sn–3.0Zr–0.7Mo–0.3Si–0.4Nb–0.35Ta wt%) fabricated by LBM could be found in the open literature [19]. The microstructure of this titanium alloy fabricated by LBM was an acicular martensitic α' phase with 0.5- μm -wide laths, and its oxidation resistance was higher than that of the as-casted alloy. But the mechanisms of oxidation and the kinetics data were poorly described. In the following paper, the effects of the specific microstructure and surface of as-built LBM samples and the high-temperature oxidation behaviour of the titanium alloy Ti–6Al–4V fabricated by LBM have been studied and compared to Ti–6Al–4V fabricated by conventional rolling. Moreover, influence of hot isostatic pressure, HIP, treatment on the microstructure and oxidation behaviour of Ti–6Al–4V fabricated by LBM has been investigated.

Experimental Procedures

Ti–6Al–4V alloy samples were produced by LBM using an EOS M280 machine equipped with an Yb-fibre laser working at a wavelength between 1060 and 1100 μm . The LBM was processed under argon atmosphere to limit thermal oxidation. Process parameters were optimized to obtain fully dense parts. The powder used, supplied by AP&C, was plasma atomized Ti–6Al–4V with a particles size of 15–45 μm and was recycled 21 times before the making of our samples. The chemical composition of the unused powder according to ASTM B348 is presented in Table 1.

Table 1 Chemical composition of Ti–6Al–4V alloys (Al, V and Fe measured by ICP-OES; C, N, O, S and H measured by IGA)

	Al	V	C	O	N	H	Fe	Other	Ti
Unused LBM powder (wt%)	6.5	3.9	0.02	0.12	0.02	0.0023	0.19	<0.4	Bal
Unused LBM powder (at.%)	10.97	3.48	0.08	0.34	0.06	0.10	0.15		Bal
LBM sample (wt%)	6.4	4.0		0.16		0.0048	0.21	<0.4	Bal
LBM sample (at.%)	10.8	3.6		0.46		0.22	0.17		Bal
Rolled sample (wt%)	6.41	3.93	0.004	0.18	0.008	0.0039	0.16	<0.4	Bal
Rolled sample (at.%)	10.82	3.51	0.02	0.51	0.03	0.18	0.13		Bal

Some of the samples were HIP-treated after LBM to reduce residual porosity thereby improving structural integrity. A rolled Ti–6Al–4V annealed above the $\alpha \rightarrow \beta$ phase transformation temperature, $T_\beta=980$ °C, was used as the reference material [20].

Spherical Ti–6Al–4V powder produced by AP&C with a particle size between 15 and 45 μm and 0.10–0.12 wt% of oxygen content according to standard ASTM E1409 was used for oxidation study.

Examination of the microstructure was done after samples were ground with SiC abrasive paper of P2400 grit size and polished with SiO_2 solution. To reveal the microstructure, samples were etched in a solution of 100 ml of water, 2 ml of HF (75%) and 4 ml of HNO_3 (65%). Two cross sections were examined to study the anisotropy of the microstructure. One is the plane parallel to the building direction, and the other one is the plane perpendicular to the building direction. Micrographs were taken using Wild M420 binocular microscope and Nikon ECLIPSE MA200 optical microscope (OM). FEI Quanta 450 and LEO 435 VP scanning electron microscopes (SEM) were used at 15 kV for high-magnification micrographs. Chemical composition was measured by inductively coupled plasma-optical emission spectrometry (ICP-OES), instrumental gas analysis (IGA) and inert gas fusion (IGF). Phases were identified by X-ray diffraction (XRD) at room temperature with a Bruker D8-2 using Cu- $K\alpha$ radiation in the 2θ range from 20° to 80° with a step size of 0.02° and a scan step time of 2 s. The relative density was measured using the Archimedes method. An average of three measurements was taken for each sample.

Nine samples were fabricated by LBM in net shape with dimensions of $15 \times 10 \times 2$ mm³. Three samples were kept in as-built LBM conditions, three samples were ground to a P600-grit finish (LBM P600), and three samples were HIP-treated and ground to a P600-grit finish (HIP P600). Three additional samples rolled and annealed above T_β were added as references materials and were also ground to a P600-grit finish (Rolled P600). Grinding was carried out to assess the influence of metallurgical state on oxidation behaviour, independently of the effect of surface roughness of as-built LBM samples.

Ti–6Al–4V samples were inserted in a pre-heated Carbolite furnace LHT 6/60 with forced convection. An opening, which allowed atmosphere renewal, was present in the top wall of the furnace. Oxidations were performed at 500, 550 and 600 °C, for 500 h and cooled at room temperature. Sample weights were measured before and after oxidation using a Sartorius® LA 75 3200D balance with an accuracy of ± 20 μg . For each of the 12 samples, weight gain values were averaged on three measurements for every oxidation condition. The samples oxidized during 500 h were prepared for microstructure characterization. Ti–6Al–4V powder was both oxidized in a SETARAM TAG24 s thermobalance at 600 °C for 100 h and in the pre-heated Carbolite furnace LHT 6/60 with forced convection at 600 °C for 300 h to study the oxidation kinetics of the powder. A mass of 7 mg of powder was used.

The thickness of the oxide layer of oxidized samples was assessed by optical microscopy measurement. For each sample, 20 images of cross sections were performed. For each image, 50 punctual measurements of oxide layer thickness were taken along the image. For each sample, oxide layer thickness corresponds to the

mean value out of these 1000 punctual measures. Oxygen concentration profiles were measured by electron probe microanalyzer (EPMA) with a CAMECA SXFive microprobe operating at 15 kV and 20 nA. Two profiles were performed on each tested sample with a standard deviation of 6000 ppm on oxygen concentration measurement. Moreover, EPMA results were corrected by removing the oxygen concentration corresponding to the non-heat-treated zone and the oxygen contamination on the surface of the sample. Oxide layers were assayed using XRD— 2θ range from 20° to 80° , step size of 0.04° , scan step time of 6 s—and energy-dispersive analysis (EDS).

Results and Discussion

Microstructure Characterization

Figure 1 shows the surface state of Ti–6Al–4V samples fabricated by LBM. Some powder grains have been partially melted and remain on the surface of the sample, thereby increasing its roughness and specific area. The relative density of samples measured using the Archimedes method is 99.5%. Sample density was determined relatively to the theoretical Ti–6Al–4V density value of 4.43 g cm^{-3} [21]. Two kinds of pores are observed in the microstructure. Figure 2a, b presents large and non-spherical pores of 10–50 μm located at 100 μm under the surface, and small and spherical pores of 2–3 μm all over the bulk.

LBM alloy microstructure was characterized before and after HIP treatment and compared to conventional alloy microstructure obtained after rolling and annealing treatment in the β field. Figure 2 shows the microstructure of Ti–6Al–4V produced by LBM. Figure 1a, c, respectively, presents a view perpendicular (XY plane) and parallel (XZ plane) to the building direction, defined as the Z axis. The XZ plane indicates that prior β grains ($130 \pm 20 \mu\text{m}$ in width) grew

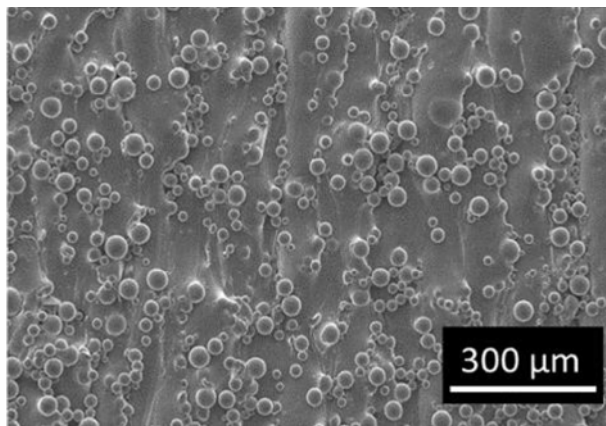


Fig. 1 Surface state of Ti–6Al–4V fabricated by LBM

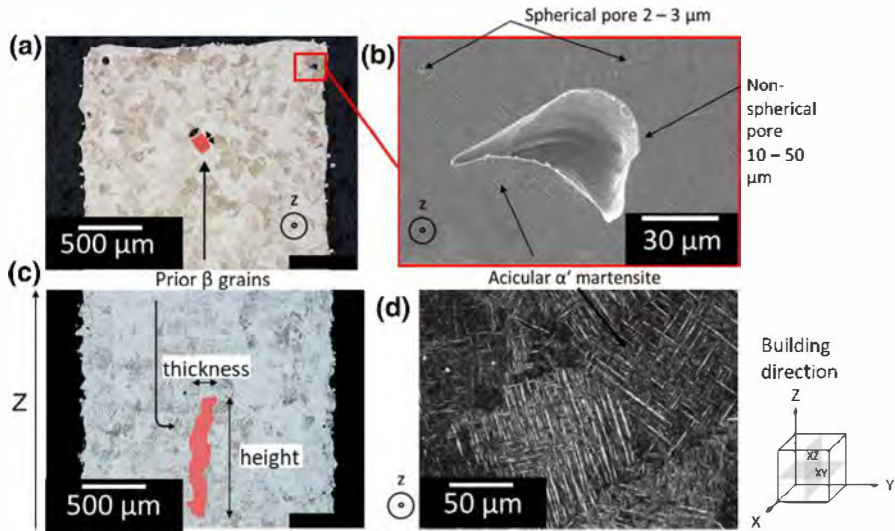


Fig. 2 Optical and high-resolution metallographic views of Ti-6Al-4V alloys fabricated by LBM. **a** prior β grain perpendicular to the building direction, **b** macroscopic and microscopic porosities, **c** elongated prior β grain parallel to the building direction and **d** acicular α' martensite

epitaxially during the process (up to $748 \pm 244 \mu\text{m}$ in length) along the building direction due to the direction of the thermal gradient. In the XY plane, the laser scanning strategy is visible with a shift between subsequent layers. Prior β grains appeared as squares of $130 \pm 30 \mu\text{m}$ in width. Figures 2b, d and 3a, respectively, show a higher magnification micrograph, a dark field optical micrograph and a bright field optical micrograph showing fully acicular α' martensitic microstructure. This microstructure was found for alloy Ti-6Al-4V built by LBM [15] due to a high cooling rate, estimated around 10^5 K s^{-1} [22]. The average width of laths obtained by the method of intercepts is $(640 \pm 130) \text{ nm}$.

The X-ray diffraction pattern in Fig. 4 indicates the presence of an hexagonal phase corresponding to the martensitic phase α' , but does not indicate the presence of β -phase.

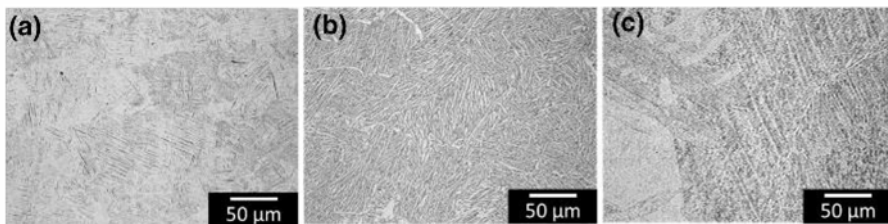


Fig. 3 Optical metallographic views of Ti-6Al-4V alloys fabricated by LBM before HIP treatment (a), fabricated by LBM after HIP treatment (b) and rolled and annealed (c)

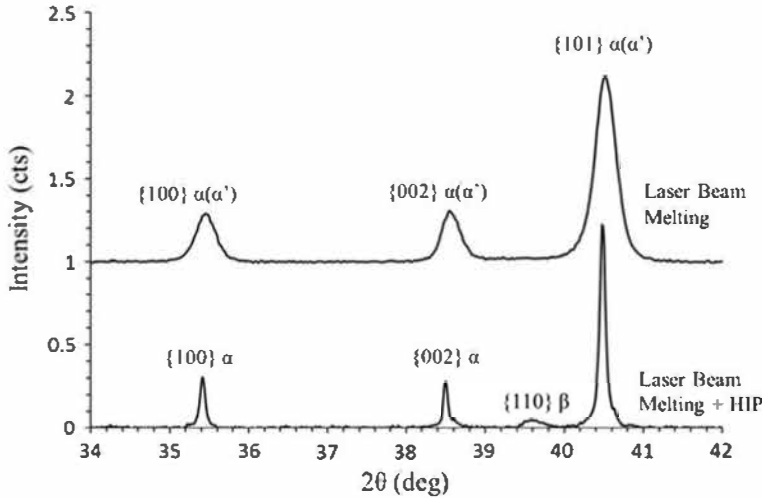


Fig. 4 X-ray diffraction pattern of Ti-6Al-4V fabricated by LBM before and after HIP treatment

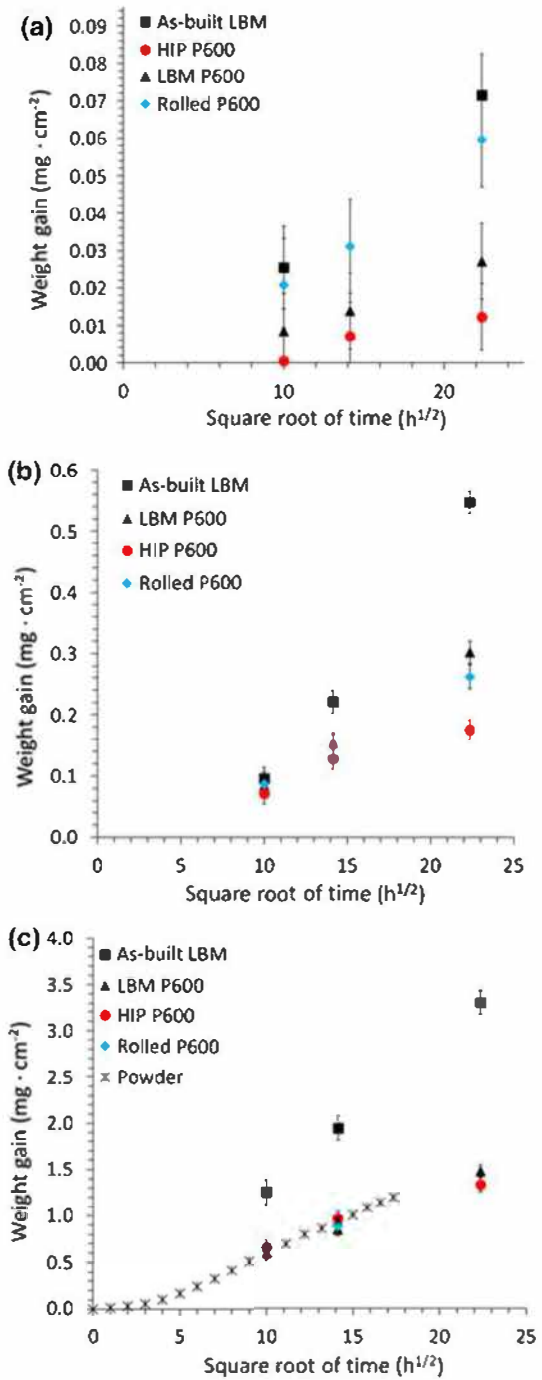
Figure 3b shows the microstructure of a sample fabricated by LBM- and HIP-treated. HIP treatment at 920 °C under 1000 bar for 2 h in argon atmosphere with a cooling rate of 4 K min⁻¹ induced the decomposition of acicular α' martensitic laths into a α + β lamellar structure with α laths of 2 ± 0.5 μm wide surrounded by β matrix. HIP treatment allowed closing the large and non-spherical pores. XRD analysis in Fig. 4 confirmed the presence of β-phase. Figure 3c shows the α + β lamellar Widmanstätten-like microstructure of the reference material fabricated by rolling followed by an annealing treatment in the β field and either an air cooling or a furnace cooling [4].

Oxidation Behaviour

Figure 5 indicates weight gains of samples after exposure to air at 500, 550 and 600 °C of Ti-6Al-4V alloys with different metallurgical and surface states. Each specimen's weight gain was divided by its specific surface area; values are expressed in mg/cm². The weight gain value of the Rolled P600 sample oxidized for 500 h at 600 °C is not included in Fig. 5c, and the weight gain value of the LBM P600 sample oxidized for 500 h at 600 °C was underestimated, both due to the spalling of the oxide layer. Figure 5a shows that weight gains of Ti-6Al-4V alloy at 500 °C are very low, and error bars show the difficulty of measuring weight gain before 500 h of oxidation due to very low weight gain values and to balance accuracy of ± 20 μg.

After 500 h of oxidation at 500, 550 and 600 °C, LBM P600 and Rolled P600 samples present a similar weight gain, as depicted in Fig. 5a-c. The metallurgical state of LBM samples exhibits oxidation kinetics similar to the rolled Ti-6Al-4V alloy used as reference material. However, HIP P600 samples present the lowest weight gain after 500 h of oxidation at every temperature. This could be due to the formation of a partially protective alumina diffusion barrier. However, this

Fig. 5 Variation of normalized weight gain ($\Delta W/A$) at 500 °C (a), 550 °C (b) and 600 °C (c) as a function of oxidation time (t) depending on surface and metallurgical state of Ti-6Al-4V alloys



assumption could not be addressed in the present work. Moreover, after 500 h of oxidation at 500, 550 and 600 °C, as-built LBM samples present a weight gain two times higher than LBM P600 samples. As shown in Fig. 1, the surface state of as-built LBM samples displays large amounts of partially melted powder particles which increase the specific area of the sample. In order to evaluate the effect of these powder particles on the surface of as-built samples, a Ti-6Al-4V powder with the same particle size as the powder on as-built LBM surfaces was oxidized. The amount of partially melted powder on as-built LBM samples was quantified by image analysis of scanning electron micrographs such as the one displayed in Fig. 1. As-built LBM samples present about 60,000 powder particles per cm² of sample surface with a diameter of 15–45 μm. Figure 5c shows the oxidation of Ti-6Al-4V powder at 600 °C for 100 h. Weight gains were calculated in proportion to the amount of powder particles present on the surface of as-built LBM samples. After 100 h at 600 °C, the weight gain of as-built LBM sample is close to the sum of the weight gain of the LBM P600 sample and of the Ti-6Al-4V powder. This proves that the higher weight gain of as-built LBM samples is mainly due to the presence of powder at the surface of the samples. These powder grains increase the surface area for oxidation, but they also oxidize faster than a flat surface, with non-parabolic kinetics as shown in Fig. 5c. Weight gain measurements for the powder oxidized during 100 h at 600 °C in the TAG apparatus showed a linear-like oxidation kinetics. Sharp et al. [23] reviewed the oxidation kinetics models for powders. They concluded that oxidation kinetics of a spherical powder can be fitted by different models where the oxidation progress is limited by the diffusion in the reaction product layer at the surface of a spherical particle (D_4) or limited by the reaction for a sphere (R_3). In both models, oxidation kinetics of the powder should be, respectively, sub-parabolic or sub-linear because the area for oxidation decreases. Figure 5c presents the oxidation kinetics of Ti-6Al-4V powder in a parabolic plot. It shows that the initial kinetics (first 100 h) is not sub-parabolic, but the kinetics increases from a parabolic rate to a linear rate. This phenomenon could be due to the cracking of powder grains, as observed in Fig. 6. After 500 h of oxidation at 600 °C, almost all oxidized powder grains are cracked. This was expected because of the anionic growth of TiO₂ oxide layer and because of the high value of the Pilling and Bedworth ratio (PBR=1.77 for Ti- α and PBR=1.74 for Ti- β in pure titanium; PBR=1.81 for

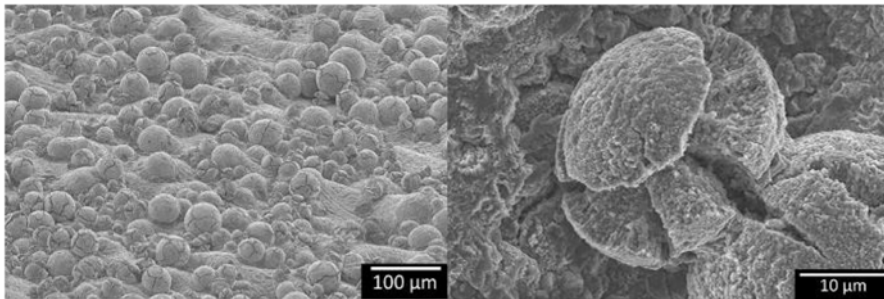


Fig. 6 Oxidized powder on as-built LBM samples oxidized 500 h at 600 °C

Ti- α and PBR=1.89 for Ti- β in Ti-6Al-4V alloy) between titanium and rutile lattices. The Pilling and Bedworth ratio (PBR) was calculated by the authors from the crystallographic data for rutile TiO₂ and Ti- α and Ti- β phases measured by XRD ($a=2.95$ Å and $c=4.68$ Å for Ti- α and $a=3.30$ Å for Ti- β in pure titanium and $a=2.92$ Å and $c=4.67$ Å for Ti- α and $a=3.21$ Å for Ti- β in Ti-6Al-4V titanium alloy). The PBR is equal to the volume of TiO₂ formed for each atom of Ti divided by the volume of a metallic site in the α or β titanium phase. And radial cracks in the rutile layer give oxygen an easy access to the unreacted core of the particles and maintain a fast reaction rate.

Figure 5 shows that oxidation kinetics can be approximated with parabolic kinetics presented in Eq. 1 and the weight gain data can be fitted as:

$$\frac{\Delta W}{A} = \sqrt{k_p \cdot t} \quad (1)$$

where k_p is the parabolic rate constant, ΔW the weight gain and t the time. A is the surface area of a sample calculated from its dimensions. For the powder, the weight gain is given for the quantity of powder present on 1 cm² of sample. Temperature dependence of the parabolic rate constant can be observed, Fig. 5, as weight gain increases with temperature. Figure 7 shows that k_p follows an Arrhenius law Eq. 2:

$$k_p = k_p^0 \cdot \exp\left(-\frac{E_a}{RT}\right) \quad (2)$$

where E_a is the activation energy, R the gas constant and T the reaction temperature.

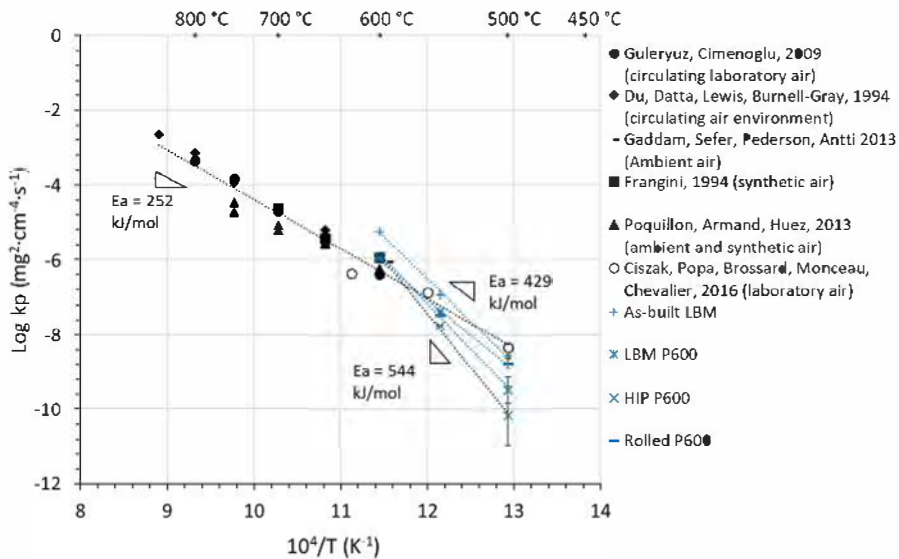


Fig. 7 Arrhenius plot of parabolic rate constant k_p for oxidation of Ti-6Al-4V alloys [3, 25–29]

Figure 7 indicates parabolic rate constant values (k_p) extracted from the literature and the present study. k_p values from the present study were obtained through the linear regression of $\frac{\Delta W}{A} = f(t^{1/2})$ curves. All k_p values from the literature were recalculated from initial weight gain values by fitting $\frac{\Delta W}{A} = f(t^{1/2})$ and forcing the fitting curve to pass through zero. In order to compare only parabolic oxidation rates, weight gain values from Guleryuz [3] above 36 h at 700 °C and the last value at 750 °C were excluded from oxidation kinetics calculations. Experimental results from this study seem to be in good agreement with the literature for oxidations at 600 °C. However, activation energies (E_a) calculated from the experimental results of this study are much higher than the activation energy obtained from literature values obtained at higher temperatures. k_p values at 500 °C present large uncertainties, which increases the error of the calculated E_a . The literature survey produces only few data that could allow us to compare our experimental data on Ti-6Al-4V for temperatures lower than 550 °C. Activation energies calculated from our experimental data at low temperatures are much higher than activation energies of oxygen diffusion in rutile ($\approx 250 \text{ kJ mol}^{-1}$ [24]) and of oxygen diffusion in titanium ($\approx 200\text{--}250 \text{ kJ mol}^{-1}$ [24]). They cannot correspond to the sum of the two phenomena—i.e. external scale formation and oxygen dissolution—which should have an activation energy value between 200 and 250 kJ mol^{-1} . Therefore, the fact that low-temperature mass gains were found lower than what was expected from the extrapolation of high-temperature values may be the sign that the composition of the external scale differs depending on temperature. We can assume for example that, at low temperatures, it could be enriched in alumina and a diffusion barrier for the diffusion of oxygen in the metal could be present. The very thin scales formed at the lowest temperatures are currently under study.

X-ray diffraction was carried out on as-built LBM sample oxidized for 500 h at 600 °C; results are summarized in Fig. 8a. Peaks of Ti- α phase are visible due to the thin thickness of the oxide layer. The oxide layer of LBM-produced Ti-6Al-4V after 500 h of oxidation at 600 °C is mainly composed of rutile (TiO_2) phase. However, some peaks can be identified as α -alumina phase (Al_2O_3). The EDS cartography, Fig. 8b, confirmed the presence of alumina in the outer oxide layer at the interface between the oxide and the environment [20, 30].

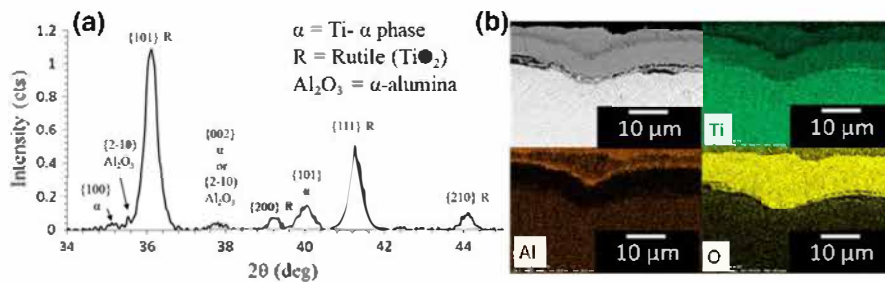


Fig. 8 X-ray diffraction pattern (a) and EDS cartography (b) of as-built LBM Ti-6Al-4V oxidized 500 h at 600 °C

Figure 9 shows Rolled P600 and HIP P600 samples oxidized for 500 h at 550 °C. A non-planar oxide layer was found on both samples at the metal/oxide and oxide/air interfaces. The scanning electron microscopy of the HIP P600 sample oxidized 500 h at 550 °C, Fig. 9c, shows a preferential oxidation appearing between the α -laths, which seem to be in the β -phase. There is still no explanation for this phenomenon which was only observed after 500 h at 550 °C.

Table 2 summarizes weight gains, parabolic rate constants k_p , oxide layer and dissolved oxygen layer thicknesses, oxide layer parabolic rate constant $k_{p(\text{oxide})}$, calculated weight gain due to the oxide layer and weight gain proportion due to dissolved oxygen ($\% \frac{\Delta W}{A}(\text{diss})$) in the metal calculated from Eq. 3 and EPMA measurements. Weight proportion due to dissolved oxygen was already calculated using oxide thickness on Ti-6Al-4V alloy (27%) [27] and with EPMA measurements on Ti6242S alloys (40–46%) [31]. Chaze and Coddet [32] calculated the ratio between the oxygen dissolved in the metallic substrate and the oxygen fixed in the aggregate (between 7 and 49% depending on titanium alloy composition) by means of microhardness measurements. However, a strong assumption of proportionality between microhardness and oxygen concentration, based on metal-oxide interface oxygen composition, was used.

$$\% \frac{\Delta W}{A}(\text{diss}) = \left(1 - \frac{\frac{\Delta W}{A}(\text{oxide})}{\frac{\Delta W}{A}(\text{total})} \right) \cdot 100 = \left(1 - \frac{\frac{e_{\text{ox}} \cdot 2 \cdot M_{(\text{O})} \cdot \rho_{(\text{TiO}_2)} \cdot 1000}{M_{(\text{TiO}_2)}}}{\frac{\Delta W}{A}(\text{total})} \right) \cdot 100 \quad (3)$$

where $\frac{\Delta W}{A}(\text{oxide})$ is the weight gain due to the oxide layer (mg cm^{-2}), $\frac{\Delta W}{A}(\text{diss})$ is the weight gain due to dissolved oxygen in the metal (mg cm^{-2}), $\frac{\Delta W}{A}(\text{total})$ is the weight gain due to the oxide layer and the dissolved oxygen in the metal (mg cm^{-2}), e_{ox} is the oxide thickness (cm), $M_{(\text{O})}$ is the oxygen molar mass (g mol^{-1}), $M_{(\text{TiO}_2)}$ is the oxide molar mass and $\rho_{(\text{TiO}_2)}$ is the oxide density (g cm^{-3}).

The oxide layer at 500 °C was too thin to be measured by optical microscopy. The parabolic rate constant of the Rolled P600 sample oxidized at 600 °C was

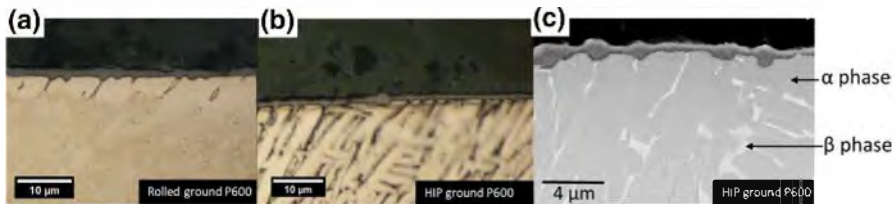


Fig. 9 Optical microscopy of rolled ground P600 (a), HIP ground P600 (b) and scanning electron microscopy of HIP ground P600 (c) oxidized 500 h at 550 °C

Table 2 Weight gains, parabolic rate constants k_p , oxide thicknesses, dissolved oxygen thicknesses, oxide layer parabolic rate constants k_p (oxide), weight gains due to oxide layer and weight gains proportion due to dissolved oxygen in the metal (*calculated with Eq. 3, **calculated with EPMA) of Ti–6Al–4V alloy oxidized for 500 h at different temperatures

	Oxidation temperature (°C)	Weight gain (mg/cm ²)	k_p (mg ² cm ⁻⁴ s ⁻¹)	Oxide thickness (μm)	Dissolved oxygen layer (ODZ) thickness (μm)	k_p (oxide) ($\times 10^{-7}$ μm ² s ⁻¹)	Weight gain due to the oxide layer at 500 h (mg/cm ²)	Weight gain proportion due to dissolved oxygen in the metal (%)
As-built LBM	500	0.072 ± 0.02	(2.7 ± 1.3) E-09	X	X	X	X	X
LBM P600		0.027 ± 0.01	(3.4 ± 4.2) E-10	X	X	X	X	X
HIP P600		0.012 ± 0.01	(6.9 ± 12) E-11	X	X	X	X	X
Rolled P600		0.06 ± 0.02	(1.7 ± 1.2) E-09	X	X	X	X	X
As-built LBM	550	0.548 ± 0.06	(1.2 ± 0.1) E-07	1.3 ± 0.5	≈ 5 μm	9.4 ± 1.4	X	X
LBM P600		0.302 ± 0.04	(4.1 ± 0.6) E-08	1.3 ± 0.2	≈ 5 μm	9.4 ± 0.3	0.22 ± 0.04	27*
HIP P600		0.175 ± 0.03	(1.8 ± 0.3) E-08	0.9 ± 0.2	≈ 5 μm	4.5 ± 0.3	0.15 ± 0.04	13*
Rolled P600		0.262 ± 0.04	(3,4 ± 0.5) E-08	1.4 ± 0.4	X	10 ± 0.8	0.23 ± 0.07	12*
As-built LBM	600	3.312 ± 0.03	(5.7 ± 0.7) E-06	8.9 ± 0.9	≈ 19 μm	440 ± 0	X	35 ± 0**
LBM P600		≈ 1.482 (small peeled off)	(1.1 ± 0.3) E-06	7.4 ± 0.8	≈ 19 μm	300 ± 0	≈ 1.3 ± 0.0	≈ 15 – 20* 35 ± 2**
HIP P600		1.338 ± 0.02	(1.1 ± 0.2) E-06	6.4 ± 0.7	X	230 ± 0	1.1 ± 0.0	17*
Rolled P600		X (half peeled off)	(1.1 ± 0.2) E-06	7.8 ± 0.6	X	340 ± 0	X	X

calculated from weight gain values obtained at 100 and 200 h because the sample was peeled off after 500 h of oxidation. Table 2 shows that weight gains, k_p , oxide layer and dissolved oxygen layer thicknesses, $k_{P(\text{oxide})}$, and weight gains due to the oxide layer all increase with temperature. $k_{P(\text{oxide})}$ and weight gains due to the oxide layer were overestimated for LBM P600 and were not calculated for Rolled P600 due to the porosity of the oxide layer and to oxide scale spalling which appeared during cooling at ambient air. After 500 h of oxidation at 550 °C, HIP P600 and Rolled P600 samples present a smaller proportion of weight gain due to dissolved oxygen (from Eq. 3) as compared to the LBM P600 sample. The presence of larger α -laths and β -phase at laths interfaces may explain these results. Moreover, LBM P600 exhibits a higher amount of α -phase, which can dissolve a higher amount of oxygen than the β -phase. After oxidation at 550 and 600 °C for 500 h, the oxide layer thickness of as-built LBM and LBM P600 samples were similar. As displayed in Fig. 1, the presence of powder grains at the surface of as-built LBM samples explains weight gain discrepancies. Finding the same oxide layer thickness on as-built and P600 samples is consistent with this result. Moreover, EPMA analysis, Fig. 10, confirmed that the presence of partially melted powder particles on the surface of as-built samples does not affect the thickness of the ODZ. As-built LBM and LBM P600 samples have the same ODZ thickness of about 20 μm for 500 h of oxidation at 600 °C. Near the metal/oxide interface, the oxygen concentration measured ranged from 25 to 27 at.% at 1–2 μm from the interface. These values are below the oxygen solubility of 33.3 at.% in Ti- α phase reviewed by Murray and Wriedt [33]. But, because of the oxygen concentration gradient, the extrapolations of these EPMA profiles at the interface ($x=0$) are not that far from the equilibrium concentration value. Note that the amount of β -phase is too low to affect significantly the interfacial oxygen concentration. The presence of alloying elements at the metal/oxide interface may also explain a lower oxygen solubility as compared to that of pure titanium. Microhardness was not used on these samples because ODZ thickness was too low.

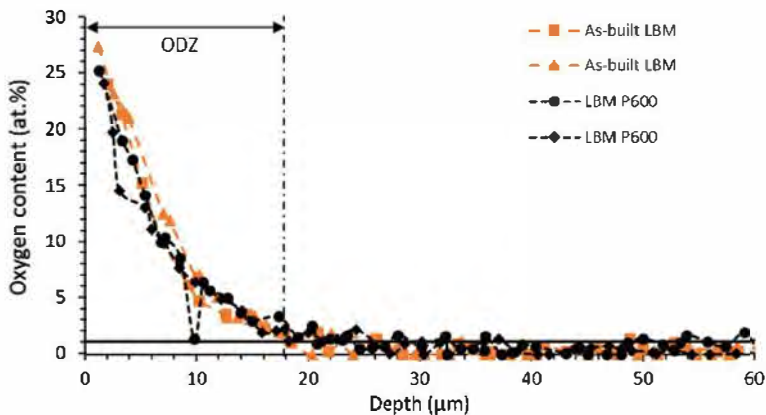


Fig. 10 EPMA profiles for oxygen in Ti-6Al-4V oxidized at 600 °C for 500 h in air

Conclusions

This study focused on the isothermal oxidation of Ti–6Al–4V alloy fabricated by laser beam melting allows the following conclusions to be drawn:

1. The microstructure of Ti–6Al–4V fabricated by LBM is composed of columnar prior β grains elongated in the building direction and fine martensite α' laths due to high cooling rate [22]. The decomposition of α' into α lamellar microstructure within the β matrix occurs during HIP treatment.
2. Thermal oxidation of as-built LBM Ti–6Al–4V alloy at 600 °C for 500 h exhibits the formation of an oxide film made of a rutile phase (TiO_2) and an α -alumina phase ($\alpha\text{-Al}_2\text{O}_3$) located at the outer scale.
3. Ti–6Al–4V fabricated by LBM and ground P600 presents oxidation kinetics at 500, 550 and 600 °C close to that of Ti–6Al–4V rolled and annealed in the β field ground P600.
4. After oxidation at 500, 550 and 600 °C, the oxidation rate of HIP P600 samples is lower than that of LBM P600 and Rolled P600 samples.
5. Rolled P600 and HIP P600 samples oxidized 500 h at 550 °C show a preferential oxidation between the α -laths where the β -phase is mainly present and a weight gain proportion due to dissolved oxygen lower than that of LBM P600 sample.
6. The surface state of samples fabricated by LBM is wavy, with partially melted powder grains increasing its specific area. For oxidations performed at 500, 550 and 600 °C, as-built LBM samples present a higher weight gain than ground samples. The difference in weight gain is predominantly due to the oxidation of powder grains located at the surface of as-built LBM samples. Both samples present similar oxide layer thickness and dissolved oxygen layer thickness. Hence, the surface state of as-built samples increases weight gain but does not increase local oxidation kinetics.

Acknowledgements This work falls within the framework of the Anddruo project hosted by the French Institute of Technology IRT Saint Exupery, supported by Occitanie Region and industrial partners.

Data Availability The raw/processed data required to reproduce these findings cannot be shared at this time as the data also form part of an ongoing study.

References

1. R. R. Boyer, *MSE A Properties Microstructure and Processing* **213**, 103 (1996).
2. P. Kofstad, K. Haufler and H. Kjøllsødal, *Acta Chemica Scandinavica* **12**, 239 (1958).
3. H. Guleryuz and H. Cimenoglu, *Journal of Alloys and Compounds* **472**, 241 (2009).
4. G. Lütjering, J. C. Williams, Titanium, 2nd edn., in *Engineering Materials and Processes*, (Springer, 2007), p. 1 & p. 203. <https://doi.org/10.1007/978-3-540-73036-1>
5. J. P. Kruth, *CIRP Annals* **40**, 603 (1991).
6. J. P. Kruth, G. Levy, F. Klocke and T. H. C. Childs, *CIRP Annals* **56**, 730 (2007).

-
7. T. Craeghs, S. Clijsters, E. Yasa, F. Bechmann, S. Berumen and J.-P. Kruth, Determination of geometrical factors in layerwise laser melting using optical process monitoring. *Optics and Lasers in Engineering* **49**, 1440–1446 (2011).
 8. C. Van Gestel, *Study of Physical Phenomena of Selective Laser Melting Towards Increased Productivity*, Ph.D. thesis, Ecole Polytechnique Fédérale de Lausanne, 2015, p. 1.
 9. L. E. Murr, S. A. Quinones, S. M. Gaytan, M. I. Lopez, A. Rodela, E. Y. Martinez, D. H. Hernandez, E. Martinez, F. Medina and R. B. Wicker, *Journal of the Mechanical Behavior of Biomedical Materials* **2**, 20 (2009).
 10. D. Gu, Y.-C. Hagedorn, W. Meiners, G. Meng, R. J. S. Batista, K. Wissenbach and R. Poprawe, *Acta Materialia* **60**, 3849 (2012).
 11. B. Song, S. Dong, B. Zhang, H. Liao and C. Coddet, *Materials & Design* **35**, 120 (2012).
 12. C. Qiu, N. J. E. Adkins and M. M. Attallah, *Materials Science and Engineering: A* **578**, 230 (2013).
 13. J. J. Beaman, H. L. Marcus, D. L. Bourell, J. W. Barlow, R. H. Crawford and K. P. McAlea, *Solid Freeform Fabrication: A New Direction in Manufacturing*, (Kluwer Academic Publishers, Dordrecht, 1997), p. 1.
 14. M. Peters, J. Kumpfert, C. H. Ward and C. Leyens, *Advanced Engineering Materials* **5**, 419 (2003).
 15. L. Thijs, F. Verhaeghe, T. Craeghs, J. V. Humbeeck and J.-P. Kruth, *Acta Materialia* **58**, 3303 (2010).
 16. M. Simonelli, Y. Y. Tse, C. Tuck, Further understanding of Ti–6Al–4V selective laser melting using texture analysis, proceedings of the Solid Freeform Fabrication Symposium, Materials (Titanium), University of Texas, Austin, August 6–8, 2011, p. 1.
 17. B. Vrancken, L. Thijs, J.-P. Kruth and J. Van Humbeeck, *Journal of Alloys and Compounds* **541**, 177 (2012).
 18. S. Zhang, Q. Wei, L. Cheng, S. Li and Y. Shi, *Materials & Design* **63**, 185 (2014).
 19. Y. Zhou, S. F. Wen, B. Song, X. Zhou, Q. Teng, Q. S. Wei and Y. S. Shi, *Materials & Design* **89**, 1199 (2016).
 20. E. Dong, W. Yu, Q. Cai, L. Cheng and J. Shi, *Oxidation of Metals* **88**, 719 (2017).
 21. L. E. Murr, S. M. Gaytan, D. A. Ramirez, E. Martinez, J. Hernandez, K. N. Amato, P. W. Shindo, F. R. Medina and R. B. Wicker, *Journal of Materials Science & Technology* **28**, 1 (2012).
 22. L. Thijs, M. L. Montero Sistiaga, R. Wauthle, Q. Xie, J.-P. Kruth and J. Van Humbeeck, *Acta Materialia* **61**, 4657 (2013).
 23. J. H. Sharp, G. W. Brindley and B. N. Narahari Achar, *Journal of the American Ceramic Society* **49**, 379 (1966).
 24. Z. Liu and G. Welsch, *Metallurgical Transactions* **19A**, 1121 (1988).
 25. H. L. Du, P. K. Datta, D. B. Lewis and J. S. Burnellgray, *Corrosion Science* **36**, 631 (1994).
 26. R. Gaddam, B. Sefer, R. Pederson and M. L. Antti, *IOP Conference Series: Materials Science and Engineering* **48**, 012002 (2013).
 27. S. Frangini, A. Mignone and F. de Riccardis, *Journal of Materials Science* **29**, 714 (1994).
 28. D. Poquillon, C. Armand and J. Huez, *Oxidation of Metals* **79**, 249 (2013).
 29. C. Ciszak, I. Popa, J.-M. Brossard, D. Monceau and S. Chevalier, *Corrosion Science* **110**, 91 (2016).
 30. A. M. Chaze and C. Coddet, *Journal of the Less-Common Metals* **157**, 55 (1990).
 31. C. Dupressoire, A. R. V. Put, P. Emile, C. Archambeau-Mirguet, R. Peraldi and D. Monceau, *Oxidation of Metals* **87**, 343–353 (2017).
 32. A. M. Chaze and C. Coddet, *Journal of Materials Science* **22**, 1206 (1987).
 33. J. L. Murray and H. A. Wriedt, *Bulletin of Alloy Phase Diagrams* **8**, 148 (1987).